Available online at www.sciencedirect.com
SCIENCE DIRECT®
Optics Communications 247 (2005) 111–124
OPTICS COMMUNICATIONS
www.elsevier.com/locate/optcom

X-ray photon correlation spectroscopy in a reflection geometry: coherence and resolution

Irakli Sikharulidze [a], Igor P. Dolbnya [b], Anders Madsen [c], Wim H. de Jeu [a,*]

[a] *FOM-Institute for Atomic and Molecular Physics, Kruislaan 407, 1098 SJ Amsterdam, The Netherlands*
[b] *DUBBLE CRG, ESRF, BP 220, 38043 Grenoble, France*
[c] *ID10A, ESRF, BP 220, 38043 Grenoble, France*

Received 12 July 2004; received in revised form 5 October 2004; accepted 9 November 2004

Abstract

In X-ray photon correlation spectroscopy (XPCS) the degree of coherence of the X-ray beam determines the contrast of the observed intensity correlation function. In this article, we present XPCS measurements of smectic liquid crystal membranes in a reflectivity geometry showing that both coherence and resolution can influence the time dependence of the correlation function. Variation of the pre-detector slits as well as of the projected coherence length on the membrane induce a time dependence of the intensity correlation function. We also treat several practical aspects and limitations we encountered during our XPCS studies. Finally the conditions for heterodyne detection at the specular ridge and homodyne detection at off-specular conditions are discussed.

PACS: 61.30.−v; 61.10.Kw; 42.25.kb
Keywords: X-ray photon correlation spectroscopy; Partially coherent radiation; Speckle; Smectic liquid crystal membranes

1. Introduction

During the last decade the development of third-generation synchrotrons made it possible to extend dynamic light scattering or photon correlation spectroscopy (PCS) into the X-ray domain [1–6]. This allowed to probe dynamics on molecular length scales as well as the use of optically dense samples inappropriate for conventional light scattering. In recent years several publications have appeared reporting results of the application of X-ray photon correlation spectroscopy (XPCS) to soft condensed matter systems [7–19]. The coherent properties of X-rays have been discussed in [20], sources of decoherence of the optics in [21]. In the absence of X-ray lasers a paramount

* Corresponding author. Tel.: +31 20 608 1234; fax: +31 20 668 4106.
E-mail address: irakli@amolf.nl (I. Sikharulidze).

0030-4018/$ - see front matter © 2004 Elsevier B.V. All rights reserved.
doi:10.1016/j.optcom.2004.11.044

problem in XPCS is to get sufficient scattered intensity. A sufficient degree of coherence can only be obtained by selecting via a pinhole the central flat wavefront from an incoherent source at large distance. For the small wavelength involved in X-rays the beam must be collimated down to micron size, which results in a large loss of intensity. In addition effects of beam damage put a limit on the incoming flux of the X-rays that can be accepted. As a consequence scattering geometries have to be used in XPCS that differ from those in conventional PCS. This has unveiled new ways in which both the coherence properties of light and the resolution of the setup influence the measurements. These effects are the main subject of this paper. In addition we discuss several other technical aspects and limitations we encountered during our XPCS studies of smectic membranes, including heterodyne vs. homodyne detection schemes.

In smectic-A liquid crystals the elongated molecules are organized in stacks of layers in which the long molecular axes are, on average, parallel to the layer normal. Hence a periodic structure exists in one dimension: the rod-like molecules form a density wave along the layer normal, while the system remains fluid in the other two directions. In smectic membranes the material is suspended over an opening in a solid frame [22]. They have a high degree of uniformity and a controlled thickness ranging from two to over thousands of layers. Smectic membranes provide excellent model systems for XPCS experiments [23–26]. The nearly perfect alignment of the smectic structure by the surfaces allows us to obtain intense and narrow reflections (see Fig. 1). This property makes smectic membranes particularly suitable for the use in a high-resolution XPCS setup. The one-dimensional ordering of the smectic layers leads to strong fluctuations in the system. Defining $u(\mathbf{r})$ as the layer displacement from its equilibrium position, $\langle u^2(\mathbf{r})$ is found to diverge logarithmically with the sample size (Landau–Peierls instability) [27], finally destroying the ordering. However, the divergence is slow, which opens the possibility to prepare finite-size samples. These fluctuations generate undulations of the membrane, which can be measured using dynamic light scattering techniques including XPCS.

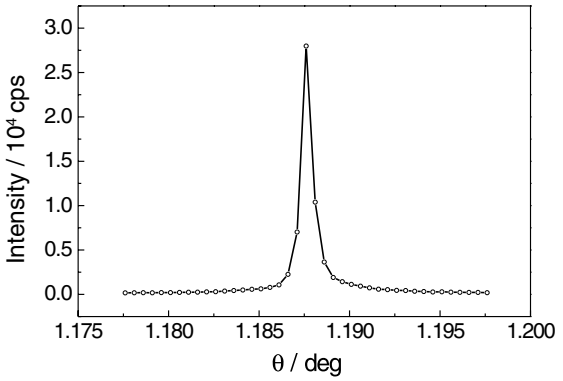

Fig. 1. Rocking curve of a 13-layer FPP membrane at the Bragg position. The almost perfect uniformity is reflected in the FWHM of 0.7 mdeg.

The intensity of X-rays scattered with a wave vector $\mathbf{q}$ is defined by the dynamic structure factor $S(\mathbf{q},t)$, which is related to the layer-displacement correlation function $\langle u(\mathbf{r}_1,0)u(\mathbf{r}_2,t)\rangle$. Because of the Landau–Peierls instability such a correlator diverges when the wave vector of the fluctuations approaches $\mathbf{q} \to 0$. To avoid this complication a cut-off parameter has been introduced, which defines the longest wavelength of the fluctuation present in the system [28]. For finite-size membranes this parameter is expected to be at the order of the lateral dimension of the membrane. However, fitting of the experimental data revealed that the cut-off value was closer to the footprint of the beam on the surface of the membrane [25,26]. This result establishes a connection with the dimension of the coherently illuminated volume of the sample from which the scattering image (speckle pattern) originates. The coherence volume is determined by the area of the sample over which the phase of the incident beam remains correlated. For a finite-size source the transverse correlation length is defined as the distance across the wavefront between points with a phase difference of π (or $\pi/2$, $\pi/4$ depending on convention). For a complex optical system the phase profile over the wavefront is more intricate. In this case one can describe the coherence properties of the beam by the complex degree of coherence $\mu(\mathbf{r}_1,\mathbf{r}_2) = \langle E(\mathbf{r}_1,t)E^*(\mathbf{r}_2,t)\rangle$. This parameter can be measured in, for instance, a double slit experiment. In that situation, the transverse

coherence length can be identified with the slit separation corresponding to the maximum of the zeroth order of $\mu(\mathbf{r}_1,\mathbf{r}_2)$. However, maxima corresponding to higher orders of $\mu(\mathbf{r}_1,\mathbf{r}_2)$ are present that manifest phase correlations in the wavefront at longer distances. The latter correlations could play a vital role as they probe fluctuations with a long wavelength that provide a dominant contribution to $S(\mathbf{q},t)$, since they diverge for $\mathbf{q} \to 0$.

The arguments given above suggest that variations of the scattering volume could lead to different relaxation profiles. In the following sections, we present several experiments illustrating this statement. First we show that variation of the detector slits results in a shift of the correlation function. Subsequently, we discuss changes of the projection of the coherence length that also induce a time dependence of intensity correlation function. Finally the question of homodyne vs. heterodyne detection will be considered.

2. Theoretical background

2.1. Coherence of X-ray radiation and XPCS

Superposition of waves with a different phase leads to the phenomenon of interference. In the classical interpretation of scattering the interference of secondary waves is considered. In the ideal case the incident wave has a constant frequency and originates from either a point source or a source at infinite distance. This means that the phases of the wave in any two points and at any two times are correlated. In reality a beam represents a superposition of waves generated by a source that is composed of many correlated or chaotic emitters positioned at a finite distance from the observer. In that situation correlations between the phase at two different points decrease for larger distances and longer time intervals between the measurements. The term coherence describes to which extent a real beam resembles a single wave and is expressed in two length scales: the longitudinal (or temporal) and the lateral coherence length. The longitudinal coherence length defines the distance between two points along the propagation direction of the beam for which the correlation between the phases is lost. An equivalent picture uses the coherence time, defined as the time interval for which correlations are lost for the phase at a fixed point. Such a decorrelation of the phases can occur as a result of the superposition of waves with different frequencies. If we define the frequency difference as $\Delta\omega$ and take waves to be out of phase for a difference of 2π, the coherence time is given by $t_{\mathrm{coh}} = 2\pi/\Delta\omega$. Depending on the convention used for the definition of the out-of-phase waves, in this definition the factor two could be removed.

XPCS experiments are based upon optical mixing as used in dynamic light scattering [29,30]. The scattered intensity is integrated out at the detector without any prior filtering. The recorded intensity is fed into a hardware autocorrelator that computes the normalized intensity correlation function,

$$g_2(\tau) = \frac{\langle I(t)I(t+\tau)\rangle}{\langle I(t)\rangle^2}, \tag{1}$$

where $I(t) = |E(t)|^2$ is the intensity at the detector. Similarly we can define

$$g_1(\tau) = \frac{\langle E(t)E^*(t+\tau)\rangle}{\langle I(t)\rangle}. \tag{2}$$

The time dependence in the field correlator in this equation is somewhat delicate. The phase of the wave in the incident beam is correlated on the scale of the coherence time t_{coh}, which is in our setup of the order of 10^{-14} s. Obviously any dynamic event to be measured is orders of magnitude slower at timescales for which the phases of the incident waves are not correlated anymore. To obtain useful information we should consider in Eq. (2) correlations of the amplitude of the scattered field only.

The wave field $E(t)$ scattered from a particular coherence volume interferes with itself but not with the field originating from neighboring volume elements. As a result, we can represent the scattering intensity as a sum of intensities scattered by each coherence region. Each component is related to the structure within the coherence volume and if this structure is changing in time the scattered intensity will also exhibit a time dependence. On the basis of this approach, we can express the

scattered intensity and the intensity correlator of Eq. (1) as

$$\begin{aligned}\langle I(t)\rangle &= \sum_{i=1}^{M}\langle I_i(t)\rangle,\\ \langle I(t)I(t+\tau)\rangle &= \left\langle \sum_{i,j=1}^{M} I_i(t)I_j(t+\tau)\right\rangle\\ &= \sum_{i=1}^{M}\langle I_i(t)I_i(t+\tau)\rangle\\ &\quad + \sum_{i=1}^{M}\langle I_i(t)\rangle\sum_{j=1}^{M}\langle I_j(t)\rangle,\end{aligned} \tag{3}$$

where M is the number of coherence regions. Furthermore we used the property that the scattered intensities from different coherence volumes are not correlated and $\langle I_i(t)I_j(t+\tau)\rangle = \langle I\rangle^2$ if $i \neq j$. According to Eq. (3) both the first, time-dependent term in $\langle I(t)I(t+\tau)\rangle$ and $\langle I(t)\rangle$ increase proportionally to the number of coherence volumes in the scattering region. Consequently $g_2(\tau)$ will decrease if the number of coherence volumes increases. Maximum performance is achieved for a spatially highly coherent beam in which the coherence and the scattering volume match.

In optical mixing experiments we can distinguish homodyne and heterodyne detection schemes. The homodyne mode works with a superposition of the scattered fields $E(t) = \sum E_s(t)$, while in heterodyne scheme the field $E_s(t)$ scattered by the sample is mixed with the field E_{ref} scattered from a local oscillator. If in the homodyne situation the fields $E_s(t)$ are statistically independent random variables, $E(t)$ will follow a Gaussian distribution that is completely characterized by its first and second moment. This implies that for the homodyne scheme the intensity correlator in $g_2(t)$ – which is a 4-field correlator – can be expressed through the 2-field correlator,

$$g_2(\tau) = 1 + |g_1(\tau)|^2. \tag{4}$$

This expression is known as the Siegert relation. It is valid for systems with many independent scatterers or when we have many coherence volumes within a scattering region (although this situation is unfavorable from the experimental point of view; see above). A direct consequence of Eq. (4) is that $g_2(\tau) \geqslant 1$. When the scatterers become correlated, collective effects come into play and Eq. (4) is not longer valid. In Section 3, we will encounter correlation functions with time intervals where $g_2(\tau) < 1$.

In the case of heterodyne mixing an additional source is present. This field E_{ref} does not depend on time and can interfere with $E_s(t)$ from the sample: $E(t) = E_{ref} + E_s(t)$. In PCS experiments a special grating is often placed in the beam to create a strong secondary source, which increases the sensitivity of the instrument. This can be seen from the expression for $g_2(\tau)$; assuming $|E_{ref}| \gg |E_s(t)|$, we can write,

$$\langle I(t)I(t+\tau)\rangle \approx I_{ref}^2 + 2I_sI_{ref}\mathrm{Re}\,[g_1(\tau)]. \tag{5}$$

Compared to the homodyne regime two points are remarkable. First we observe in heterodyne regime $g_1(\tau)$ and not its squared value. This has a direct implication on the relaxation time observed in the homodyne and heterodyne detection schemes. Particularly, if $g_1(\tau)$ decays exponentially with the relaxation time τ, than in homodyne experiment based on Eq. 4 we would observe the relaxation time $\tau/2$, while in heterodyne mode according to Eq. (5) we would detect time τ [31]. In Section 4.3, we would use this fact in the interpretation of the experimental data. Second the intensity of the local oscillator amplifies the contribution of the weakly scattered signal, which makes heterodyne detection the preferred choice in PCS. As we shall see in Section 4.3 this increase in intensity does not necessary lead to an increase in contrast of the correlation function.

The static reference field does not necessarily have to be external but can come from the sample itself. If we can separate the scattered intensity from the sample into a time-dependent and a time-independent part, similar arguments as used above can be applied [32]. A linear dependence exists between the scattered field and the electron-density profile of the sample, which can be expressed in the form,

$$E(\mathbf{q},t) = \int \mathrm{d}\mathbf{r}\rho(\mathbf{r},t)R(\mathbf{q},\mathbf{r})\mathrm{e}^{-\mathrm{i}(\mathbf{q}\cdot\mathbf{r})}, \tag{6}$$

where $R(\mathbf{q},\mathbf{r})$ includes resolution-dependent factors and possible Fresnel corrections [33]. If we split

the density into a time-dependent and a time-independent part $\rho(\mathbf{r},t) = \rho_0(\mathbf{r}) + \Delta\rho(\mathbf{r},t)$, we can decompose the scattered field $E(\mathbf{q},t)$ into two components. The first part is defined by the average distribution of the scatterers and thus will be time-independent. The second term accounts for the deviation of the scatterers from their average positions, resulting in the time-dependent component. Obviously the two components interfere with each other thus fulfilling the requirements for heterodyne detection. The consequences for the geometries chosen in the experiments on smectic membranes (for example at the quasi-Bragg position and off-specular) will be discussed in Section 4.3.

A more rigorous description of the scattering of partially coherent light can be given using the mutual coherence function $\mu(\mathbf{r}_1,\mathbf{r}_2) = \langle E(\mathbf{r}_1,t)E^*(\mathbf{r}_2,t)\rangle$ that can be represented in the following form [33]:

$$\begin{aligned}\mu(\mathbf{r}_1,\mathbf{r}_2) &= \langle E(\mathbf{r}_1,t)E^*(\mathbf{r}_2,t)\rangle \\ &= \Psi(\mathbf{r}_1)\Psi(\mathbf{r}_2)g(\mathbf{r}_1-\mathbf{r}_2)I/A. \end{aligned} \tag{7}$$

Here, A is the scattering area to be integrated over, $\Psi(\mathbf{r})$ is an amplitude factor and $g(\mathbf{r}_1-\mathbf{r}_2)$ a coherence factor. The latter can be related to the transverse coherence lengths ξ_x and ξ_y according to

$$g(\mathbf{r}_1-\mathbf{r}_2) = \exp\left(-\frac{(x_1-x_2)^2}{2\xi_x^2}\right)\exp\left(-\frac{(y_1-y_2)^2}{2\xi_y^2}\right). \tag{8}$$

Using Eq. (7) we can write the structure factor $S_t(\mathbf{q})$ at time t in the following form:

$$\begin{aligned}S_t(\mathbf{q}) = \int \mathrm{d}\mathbf{r}_1\,\mathrm{d}\mathbf{r}_2 \mathrm{e}^{-\mathrm{i}\mathbf{q}(\mathbf{r}_1-\mathbf{r}_2)}\Psi(\mathbf{r}_1)\Psi(\mathbf{r}_2)g(\mathbf{r}_1-\mathbf{r}_2) \\ \times F(\mathbf{r}_1,\mathbf{r}_2)\langle\rho(\mathbf{r}_1)\rho(\mathbf{r}_2)\rangle, \end{aligned} \tag{9}$$

where $F(\mathbf{r}_1,\mathbf{r}_2)$ contains the Fresnel phase factors [33]. Note that this is not a time-averaged expression but refers to the scattered intensity $I(t)$ at a particular time t. In order to include the finite resolution of the setup, we must convolute $S_t(\mathbf{q})$ with the resolution function $R(\mathbf{q})$ that defines the range of scattering vectors $(\Delta q_x,\Delta q_y)$ probed at momentum transfer q.

The Fourier transform $\widetilde{R}(\mathbf{r}_1-\mathbf{r}_2)$ of the resolution function can be expressed in a Gaussian form as [34],

$$\begin{aligned}\widetilde{R}(\mathbf{r}_1-\mathbf{r}_2) = \exp\left(-\frac{1}{2}\Delta q_x^2(x_1-x_2)^2\right) \\ \times \exp\left(-\frac{1}{2}\Delta q_y^2(y_1-y_2)^2\right) \end{aligned} \tag{10}$$

and this form can be incorporated into the expression for $S_t(\mathbf{q})$:

$$\begin{aligned}S_t(\mathbf{q}) = \int \mathrm{d}\mathbf{r}_1\,\mathrm{d}\mathbf{r}_2 \mathrm{e}^{-\mathrm{i}\mathbf{q}(\mathbf{r}_1-\mathbf{r}_2)}\Psi(\mathbf{r}_1)\Psi(\mathbf{r}_2)g(\mathbf{r}_1-\mathbf{r}_2) \\ \times \widetilde{R}(\mathbf{r}_1-\mathbf{r}_2)F(\mathbf{r}_1,\mathbf{r}_2)\langle\rho(\mathbf{r}_1)\rho(\mathbf{r}_2)\rangle. \end{aligned} \tag{11}$$

The coherence volume is defined through $g(\mathbf{r}_1-\mathbf{r}_2)$ and $\widetilde{R}(\mathbf{r}_1-\mathbf{r}_2)$ by the transverse 'incident' coherence lengths ξ_x and ξ_y. Note that the coherence of the radiation at some point $\mathbf{r}$ is defined by the whole optical system [20]. From Eqs. (8), (10) and (11), we note that the coherence properties of the incident beam and the resolution of the setup have a similar influence on the scattering function. Hence, we can combine in an heuristic way $g(\mathbf{r}_1-\mathbf{r}_2)$ and $\widetilde{R}(\mathbf{r}_1-\mathbf{r}_2)$ into an 'effective' resolution of the setup given by

$$\begin{aligned}\Delta' q_x^2 &= \Delta q_x^2 + 1/\xi_x^2, \\ \Delta' q_y^2 &= \Delta q_y^2 + 1/\xi_y^2. \end{aligned} \tag{12}$$

In Section 4.1, we will present experiments displaying the effects of resolution changes and modifications of the coherence volume on the XPCS data.

2.2. Dynamics of fluctuations in smectic membranes

A smectic liquid crystal membrane can be represented as a stack of liquid layers at an average position $z + nd$. The density distribution in such a stack can be written as a convolution of the single layer density profile $\rho_z(z)$ with the actual layer position [28]:

$$\rho(\mathbf{R},t) = \int \mathrm{d}z'\rho_s(z')\sum_{n=0}^{N}\delta(z'-(z+nd)-u_n(\mathbf{r},t)), \tag{13}$$

where $\mathbf{R} = (\mathbf{r},z)$. Using this form we can translate density fluctuations in terms of the correlator of the layer displacements, which can be expressed in a Fourier form as [35]:

$$\langle [u(\mathbf{r}_1,0)-u(\mathbf{r}_2,t)]^2\rangle = \frac{1}{(2\pi)^2}\int_{2\pi/\Lambda}^{2\pi/b} \mathrm{d}\mathbf{q}_\perp (G(q_\perp,0) - J(q_\perp|\mathbf{r}_1-\mathbf{r}_2|)G(q_\perp,t)). \tag{14}$$

Now $G(q_\perp,t) = \langle u^*(-q_\perp,0)u(q_\perp,t)\rangle$ is the correlator of a single Fourier component of the layer displacement fluctuations with wave vector $q_\perp$. The upper integration limit is given by the intermolecular distance b. On this scale the continuum theory used to describe the fluctuations of the smectic layers breaks down. The presence of the lower limit in the integral is related to the Landau–Peierls instability. The divergence of the fluctuations is restricted by the finite size of the sample. In the present case, the cut-off parameter Λ is related to the lateral size of the smectic membrane.

In the high-compressibility limit all the layers in a membrane undulate 'unisono' and the layer displacement $u(\mathbf{r},t)$ depends only on the lateral coordinates. In this case $G(q_\perp,t)$ can be written as

$$G(q_\perp,t) = \frac{k_B T\tau_1\tau_2}{L\rho_0(\tau_1-\tau_2)}\left[\tau_1 \exp\left(-\frac{|t|}{\tau_1}\right) - \tau_2 \exp\left(-\frac{|t|}{\tau_2}\right)\right], \tag{15}$$

where $k_B T$ is the Boltzman factor, L the thickness of the membrane and ρ_0 the density. The times τ_1 and τ_2 are determined by the dispersion relation,

$$\frac{1}{\tau_{1,2}} \approx \frac{\eta_3 q_\perp^2}{2\rho_0}\left(1 \mp \mathrm{i}\sqrt{\frac{8\rho_0\gamma}{q_\perp^2\eta_3^2 L}-1}\right) \equiv a(q_\perp)(1 \mp \mathrm{i}f(q_\perp)). \tag{16}$$

Here, η_3 is the layer shear viscosity coefficient and γ the surface tension. Introducing relaxation times in the form given in Eq. (16) into Eq. (15) in case of the small $q_\perp$ we find that $f(q_\perp)$ is real and Eq. (15) can be rewritten as

$$G(q_\perp,t) = \frac{\mathrm{e}^{-a(q_\perp)t}}{a^4(q_\perp)f(q_\perp)[1+f^2(q_\perp)]^{\frac{3}{2}}} \times \sin\{a(q_\perp)f(q_\perp)t + \arctan[f(q_\perp)]\}. \tag{17}$$

In this situation the relaxation behavior shows a combination of exponential decay and oscillations. For large $q_\perp$, $f(q_\perp)$ becomes imaginary and we can express $G(q_\perp,t)$ as

$$G(q_\perp,t) = \frac{\mathrm{e}^{-a(q_\perp)t}}{a^4(q_\perp)|f(q_\perp)|\left[1-|f(q_\perp)|^2\right]^{\frac{3}{2}}} \times \sinh\{a(q_\perp)|f(q_\perp)|t + \operatorname{arctanh}[|f(q_\perp)|]\}. \tag{18}$$

In the situation described by this equation the fluctuations exhibit a pure exponential damping.

Fig. 2 summarizes the dependence of the relaxation time on the wave vector of the fluctuation according to Eq. (16) for typical smectic parameters [22]. For fluctuations with a small wave vector the effect of inertia results in an oscillatory damping and the relaxation times $\tau_{1,2}$ are complex conjugate values. The transition point is defined by the cross-over value $q_{\perp,c}$ where the relaxation times $\tau_{1,2}$ become real. Above this value the fluctuations show an overdamped relaxation. Depending on the experimental situation the intensity correlation function is dominated by either oscillatory or overdamped fluctuations, resulting in oscillatory or exponential decay of the intensity correlation function, respectively [25].

In actual experiments the parameter Λ introduced in Eq. (14) has been found to represent the largest relevant wavelength from the full fluc-

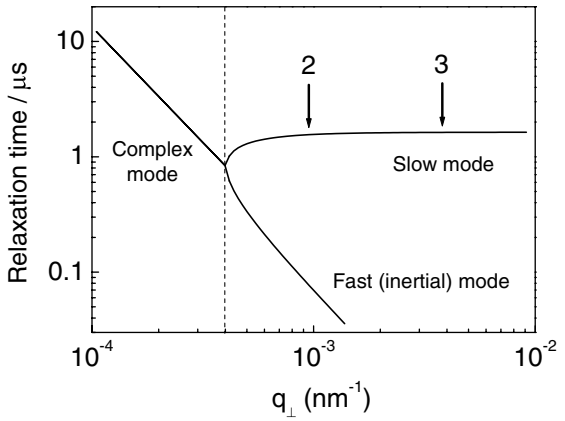

Fig. 2. Dispersion curve of the relaxations of a smectic membrane; $q_\perp$ is the wave vector of the fluctuations.

tuation spectrum [25]. It has a direct influence on the time profile of the intensity correlation function. According to Fig. 2, in the complex mode the relaxation time of a specific fluctuation increases with the wavelength. Hence a larger value of Λ leads to the shift of the correlation function to the longer times. As we shall see the choice of the relevant value of Λ is of major importance in the interpretation of the XPCS data on smectic membranes.

3. Experimental

XPCS experiments have been performed at the undulator beamline ID10A (Troïka I) of the European Synchrotron Radiation Facility (ESRF, Grenoble). The measurements have been carried out in the uniform filling mode of the storage ring (992 bunches at intervals of 2.8 ns). Time interval between bunches in the storage ring give a fundamental time limit for XPCS measurements. Preliminary collimation is done by a set of preliminary slits of 300×300 μm^2 and 200×200 μm^2 at 33 and 43 m from the source, respectively. A single-bounce Si(111) monochromator operating in a horizontal scattering geometry selects energies of 8 or 13.4 keV, corresponding to the third and fifth harmonic of the undulatior radiation, leading to a wavelength λ of 0.155 or 0.925 nm, respectively. Subsequently, the beam is reflected by a Si mirror to suppress higher order harmonics. The sample position is at a distance of 45 m from the source with full-width-at-half-maximum (FWHM) dimensions of 928×23 μm^2 (H × V). The transverse coherence length, taken as $\lambda R/s$, in which R the distance between the source and the sample and s the size of the source, is $\lessapprox 10$ μm in the horizontal direction (ξ_H) and $\gtrapprox 100$ μm in the vertical direction (ξ_V). A compound refractive beryllium lens is used to increase the incident intensity by focusing the beam in the vertical direction. Focusing reduces ξ_V, matching it to the coherence length ξ_H in the horizontal direction. The longitudinal coherence length ξ_l of about 1.5 μm is determined by the bandpass of the monochromator $\Delta\lambda/\lambda \approx 10^{-4}$.

We used 10 and 100 μm pinholes in front of the sample to select the spatially coherent part of the beam. The beam incident on the sample was observed to be structured. These distortions are attributed to speckles occurring from imperfections in the windows and other optical elements in the beam path, and cause some uncertainty in the spatial coherence lengths of the beam. Guard slits were placed after the pinhole to remove parasitic scattering. The coherent photon flux at the sample was for a 10 μm pinhole about 1×10^9 counts s^{-1}/100 mA at 8 keV and about 3×10^7 counts s^{-1}/100 mA at 13.4 keV. Fig. 3 gives the scattering geometry.

A fast avalanche photodiode (Perkin Elmer C30703) [36] with an intrinsic time resolution $\lesssim 4$ ns was used as detector at a distance of 1.5 m from the sample, with pre-detector slit gaps varying from 0.01 to 0.2 mm. The resolution of the setup was estimated as $\Delta q_x \approx 10^{-4}$ nm^{-1} and $\Delta q_y = \Delta q_z \approx 10^{-3}$ nm^{-1}. The intensity–intensity time auto-correlation function was measured in real time using a hardware multiple-tau digital autocorrelator FLEX01-8D (correlator.com, sampling time down to 8 ns). Thanks to the perfect match between the millidegree mosaicity of the smectic membranes and the high resolution of the setup we could reach count rates in the range of tens of MHz.

We have studied membranes of three smectic-A compounds: 4-octyl-4′-cyanobiphenyl (abbreviated as 8CB), *N*-(4-*n*-butoxybenzilidene)-4-*n*-octy-

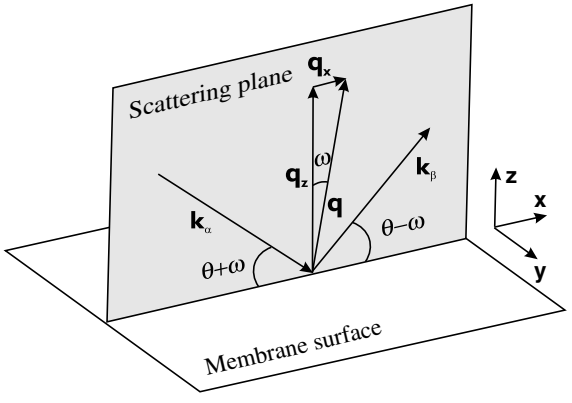

Fig. 3. Scattering geometry.

laniline (4O.8) and 4-heptyl-2-[4-(2-perfluorhexyl-ethyl)phenyl]-pyrimidin (FPP). Structural formulas and transition temperatures have been given in [25,26]. The measurements were done at temperatures at the lower end of the smectic-A range, at $T = 27$ °C for 8CB, at $T = 50$ °C for 4O.8 and at $T = 100$ °C for FPP. Membranes were stretched to about 5–10 mm using 15 and 25 mm wide frames with movable blades. For the XPCS measurements they were placed inside a two-stage oven with thin kapton windows. The oven was pumped down to 10^3 Pa to prevent parasitic X-ray scattering from air and possible sample degradation. Membrane thicknesses in the range of 0.5–20 μm were determined by optical reflectometry [37,38] and up to 3 μm from the interference fringes measured by specular X-ray reflectivity.

4. Results and discussion

4.1. Resolution effects from the pre-detector slits

In this section, we illustrate the influence of the resolution of the setup on the time dependence of the intensity relaxation function at the quasi-Bragg peak of FPP ($q_0 = 2.14$ nm^{-1}) by changing the detector slit in either the horizontal or the vertical direction. A first set of measurement was made with a 10-μm pinhole and a horizontal scattering plane (vertical membrane). The results are displayed in Fig. 4. Opening of the horizontal detector slit results in a strong loss of contrast and a shift of the correlation function towards longer relaxation times. On the other hand opening the vertical (out-of-plane) detector slit leads only to minor changes. Similar results are found in the case of a horizontal membrane (vertical scattering plane), in which the horizontal and vertical slits switch over their roles. In Fig. 5, we give results for a 100-μm pinhole (vertical membrane). In this case both the vertical and the horizontal slit influences the correlation function, slowing down the correlation time while also the contrast diminishes.

In order to quantify the observed changes one could attempt a direct fit to Eq. (17) for $G(q_\perp,t)$. However, because of the complicated intrinsic q-dependence, which has to be integrated out, we started with a more empirical approach based on a similar functional dependence (oscillatory relaxation):

$$\langle I(\mathbf{q},0)I(\mathbf{q},t)\rangle = A\exp(-t/\tau)\sin(\omega t+\phi). \qquad (19)$$

Here A, τ, ω and ϕ are fitting parameters representing contrast, relaxation time, frequency and phase. The results for the curves from Fig. 4 and Fig. 5 are given in Table 1 and Table 2, respectively. The frequency of the oscillatory part is constant for vertical membranes. On the other hand the phase factor remains overall constant within the experimental accuracy. The results for contrast and relaxation times can be summarized as follows:

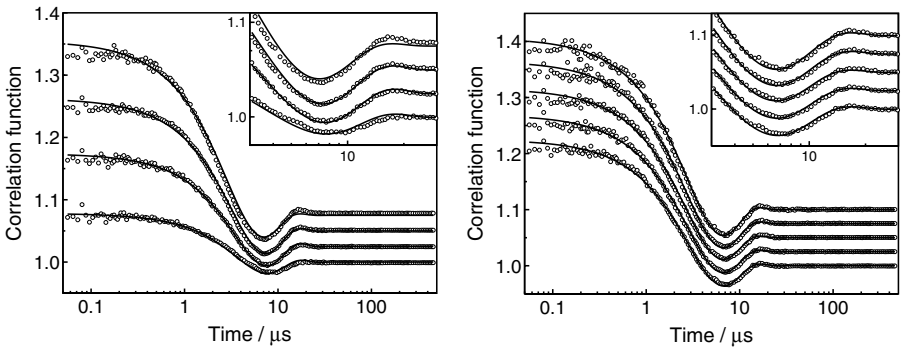

Fig. 4. Correlation functions from a 1.7-μm vertical FPP membrane (10-μm pinhole). Left: vertical slit fixed at 0.02 mm, horizontal slit (from top to bottom): 0.03, 0.06, 0.1, 0.2 mm. Right: horizontal slit fixed at 0.02 mm, vertical slit (from above): 0.01, 0.03, 0.06, 0.1, 0.2 mm. Fit parameters in Table 1.

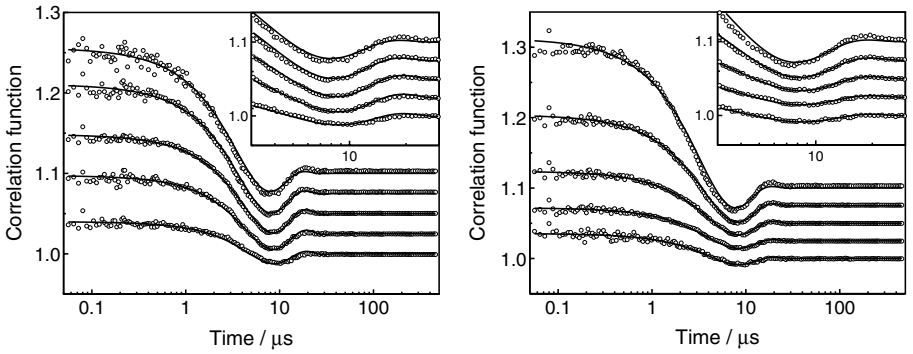

Fig. 5. Correlation functions from a 1.4-μm vertical FPP membrane (100-μm pinhole). Left: vertical slit fixed at 0.02 mm, horizontal slit (from top to bottom): 0.01, 0.03, 0.06, 0.1, 0.2 mm. Right: horizontal slit fixed at 0.02 mm, vertical slit (from top to bottom): 0.01, 0.03, 0.06, 0.1, 0.2 mm. Fit parameters in Table 2.

Table 1
Fitting parameters to Eq. (19) for the correlation functions of the vertical FPP membrane of Fig. 4 (10 μm pinhole)

In-plane slit/mm	$A \pm 0.01$	$(\tau \pm 0.1)/\mu s$	Out-of-plane slit/mm	$A \pm 0.01$	$(\tau \pm 0.1)/\mu s$
0.03	0.29	3.8	0.01	0.33	3.9
0.06	0.22	4.6	0.03	0.31	3.9
0.1	0.16	5.2	0.06	0.29	3.9
0.2	0.08	5.7	0.1	0.26	4.0
			0.2	0.24	4.0

Left: vertical slit fixed at 0.02 mm. Right: horizontal slit fixed at 0.02 mm; $\omega = 0.30 \pm 0.02\ \mu s^{-1}$, $\phi = 1.9 \pm 0.1$.

Table 2
Fitting parameters to Eq. (19) for the correlation functions of the vertical FPP membrane of Fig. 5 (100 μm pinhole)

In-plane slit/mm	$A \pm 0.01$	$(\tau \pm 0.1)/\mu s$	Out-of-plane slit/mm	$A \pm 0.01$	$(\tau \pm 0.1)/\mu s$
0.01	0.16	4.6	0.01	0.22	4.3
0.03	0.14	5.3	0.03	0.13	5.3
0.06	0.1	6.5	0.06	0.08	6.0
0.1	0.07	7.1	0.1	0.05	6.1
0.2	0.04	7.8	0.2	0.04	6.5

Left: vertical slit fixed at 0.02 mm. Right: horizontal slit fixed at 0.02 mm; $\omega = 0.29 \pm 0.02\ \mu s^{-1}$, $\phi = 1.8 \pm 0.1$.

- For the 10-μm pinhole increasing the in-plane pre-detector slit leads to: (i) an important loss of contrast, and (ii) an increase of the relaxation time. Increasing the out-of-plane detector slits gives: (i) a small but significant decrease of contrast and (ii) no change of the relaxation time. These results are independent on whether the scattering plane is horizontal or vertical. Note that a decrease of contrast is not necessarily connected with a variation of the correlation time.
- For the 100-μm pinhole the initial contrast is less than in the previous case. Upon increasing the width of a pre-detector slit (either in-plane or out-of-plane) the contrast is strongly reduced and the relaxation time increases.

The size of the 10-μm pinhole is less or about equal to the vertical and horizontal coherence length, respectively. Hence the radiation passed through has approximately symmetric coherence. For in-plane scattering the projection of the

coherence length ξ_x on the surface of the membrane is at the quasi-Bragg angle about 300 μm (the size of the footprint of the beam). In the out-of plane direction it is still about the size of the pinhole. In the latter direction one or just a few speckles are accepted by the detector and further opening of the vertical slit leads to a moderate decrease in contrast. However, in the scattering plane at least ten times more speckles will be received by the detector, and further opening will strongly reduce the contrast which in fact almost disappears. The 'effective' resolution $\Delta q_x'$ Eq. (12) is determined by the largest of the two values $1/\xi_x \leqslant 10^{-5}$ nm^{-1} and $\Delta q_x \simeq 10^{-4}$ nm^{-1}. Hence for in-plane scattering $\Delta q_x'$ is mainly determined by the resolution of the setup. When we open the detector slits we increase the resolution, and thus the cut-off wavelength Λ, leading to a larger relaxation time.

For in-plane scattering, in the case of a 100-μm pinhole we have factor 10 larger footprint than for a 10-μm pinhole. However, the projection of the coherence length ξ_x on the surface of the membrane is still about the same. Hence we can apply essentially the same arguments as in the 10-μm case. For the out-of-plane scattering the beam size is now about 100 μm while the coherence length is of the same order. This brings the out-of-plane behavior to the same scale as discussed for the in-plane scattering, resulting in the similar behavior observed experimentally. In conclusion, these results illustrate that in the present coherent experiments the whole set-up after the pinhole should be considered as 'sample'.

4.2. Dependence of the relaxation on q_z

So far we have been working exclusively at the quasi-Bragg peak corresponding to the layer structure of the smectic membranes. Moving along the specular ridge provides a means of varying the projection of the beam (and thus of the coherence length) on the surface of the membrane. To achieve a high enough count rate at different specular positions, we measured a relatively thin 13-layer 4O.8 membrane, giving broad Kiessig fringes (see Fig. 6(a)). Correlation functions taken at the maxima of the Kiessig fringes and at the quasi-Bragg position are shown in Fig. 6(b). The results of fitting the data to Eq. (19) are displayed in Fig. 6(c), and indicate shorter relaxation times as we move towards larger scattering angles. Finally Fig. 6(d) shows an increase in contrast parallel to the variation of the relaxation time with q_z.

The results can easily be understood within the framework of our model given in the previous section. For in-plane scattering now the projection on the membrane surface of both ξ_x and $1/\Delta q_x$ varies inversely proportional to q_z. Hence it does not matter which quantity is dominant. This projection directly determines the cut-off parameter Λ which decreases with increasing scattering angle leading to the observed shift of the correlation function towards faster times. Comparing Figs. 6(a) and (d) we note that the contrast increases with decreasing intensity of the Kiessig fringe (or quasi-Bragg peak). We shall return to this point in Section 4.3.

Another potential possibility to vary q_z is to work at the position of the second-order quasi-Bragg peak. In FPP the presence of fluorine leads to an increased intensity ratio of the second and first quasi-Bragg peak of about 10^{-4}, which is for other liquid crystals usually about 10^{-6}–10^{-7}. This allowed us to measure correlation functions at both the first- and the second-order Bragg position of a thick FPP membrane, shown in Fig. 7. At these positions both the illuminated footprint and the coherence volume differ by a factor two. The same applies to Λ and at the second quasi-Bragg position we should probe maximum fluctuations with a twice shorter wavelength than at the first one. The data show at the first Bragg peak oscillatory relaxation (complex mode, see Fig. 2), and at the second Bragg peak a pure exponential relaxation. As the latter slow-mode relaxation time does not depend on the wavelength of the fluctuations, we cannot decide on an exact factor of two difference in Λ. However, the change in mode is important, as this is the only example of FPP showing exponential relaxation on the specular ridge.

4.3. Homodyne/heterodyne detection

As mentioned in Section 2.1 the density of a fluctuating smectic membrane can be decomposed into a time-independent (average) part and a time-

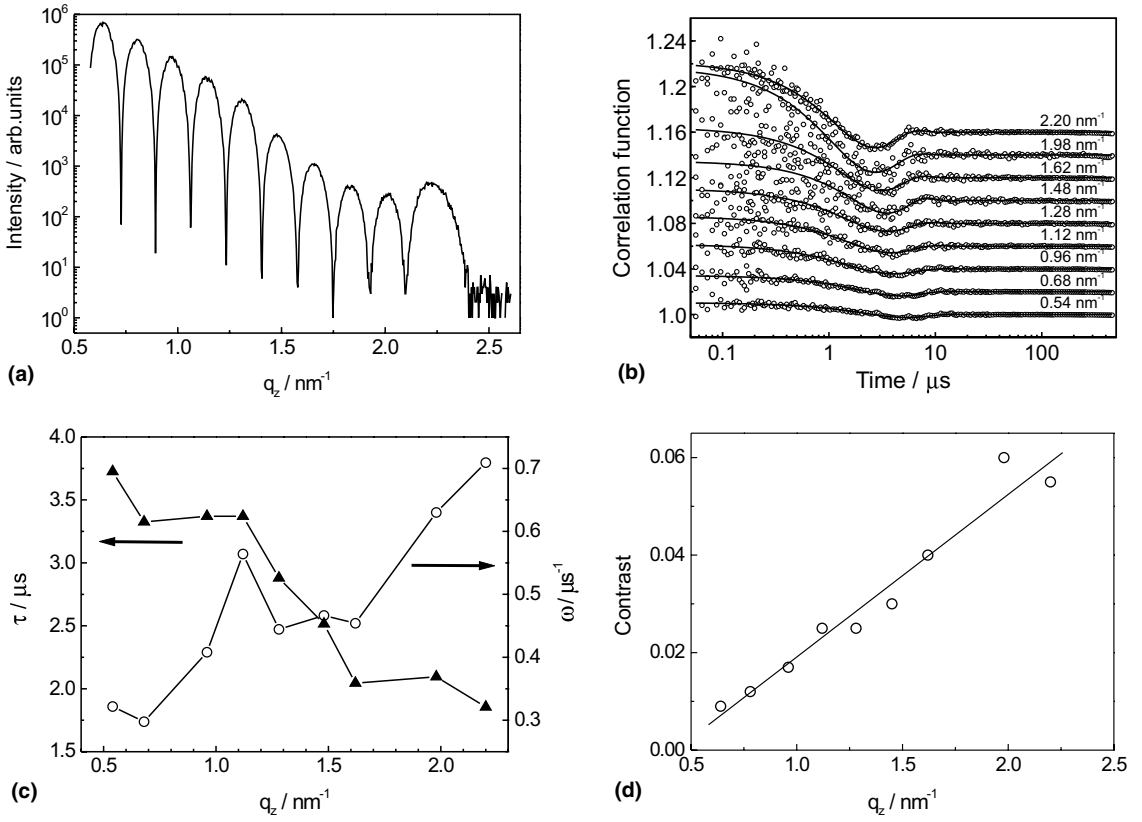

Fig. 6. Results for a 13-layer 4O.8 membrane at different specular positions: (a) reflectivity curve; (b) correlation functions (10-μm pinhole) taken at the maxima of the Kiessig fringes (shifted along the vertical axis with values of q_z indicated); (c) dependence of the fitting parameters τ (triangles) and ω (circles) on the position along the specular ridge; (d) ibid for the contrast.

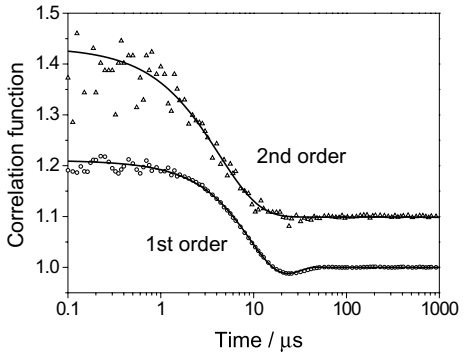

Fig. 7. Correlation functions of a 13.2-μm FPP membrane (10-μm pinhole) at the first and the second Bragg position.

dependent one. This is reflected in the scattered field that can be written as $E(\mathbf{q},t) = E_{\mathrm{ref}}(\mathbf{q}) + E_s(\mathbf{q},t)$. The last term E_s accounts for the deviation of the scatterers from their average positions reflected in E_{ref}, resulting in the time-dependent component. At the quasi-Bragg position (or more general at the specular ridge) a strong elastic component is present and the dominant term in the correlator is the cross product of the elastic and the quasi-elastic component. As a result, the intensity correlator $\langle I(t)I(t+\tau)$ depends linearly on $g_1(t)$. Hence, we have in this case a heterodyne detection scheme and the relaxation time τ obtained from fitting the intensity correlation function by Eq. (19) defines the relaxation time of $g_1(t)$. In contrast, at far off-specular positions we do not catch the static component and we are dealing with homodyne detection. In this case we can apply the Siegert relation, in which the intensity correlator is proportional to $g_1^2(t)$. In the exponential relaxation model of Eq. (19), taking the square of $g_1(t)$ results in a decrease of the relaxation time

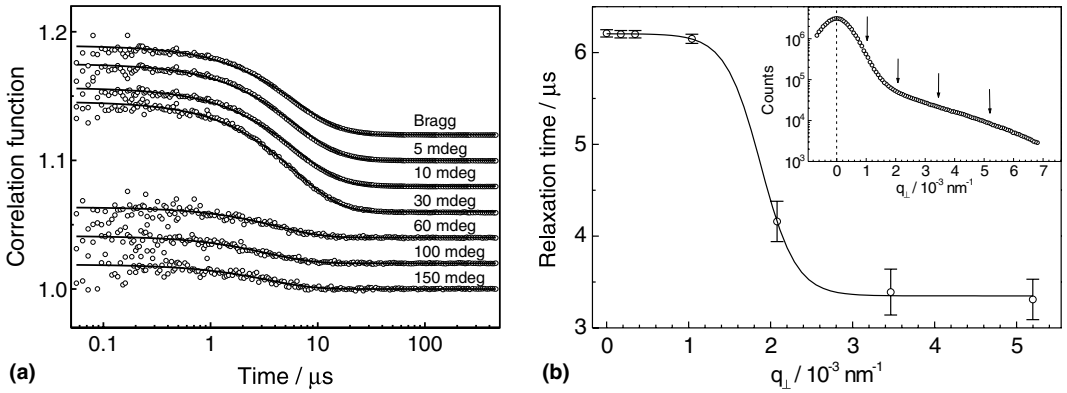

Fig. 8. XPCS measurements of a 3.8-μm 8 CB membrane at specular and off-specular positions: (a) correlation functions at the positions indicated above each curve; (b) variation of the relaxation times as a function of the offset. Inset: rocking curve with arrows indicating the measurement positions.

by a factor 2. As a result the measured relaxation time for $g_1(t)$ and for the density fluctuations becomes equal to $\tau/2$. As discussed elsewhere [39] similar considerations can be applied to the oscillating part of the correlation function. This results for the heterodyne situation in the sin-dependence of Eq. (19) and Figs. 4 and 5, while for the homodyne case a $\sin^2$-behavior of the oscillations is expected.

Fig. 8(a) shows some typical experimental results. Around the quasi-Bragg position we observe a specular relaxation time of 6.2 μs. After passing a threshold the correlation function transforms into another form with a different relaxation time. This transition manifests the switch from heterodyne to homodyne detection as the contribution of I_{ref} disappears. The threshold is determined by the angle for which the specular reflection falls on the edge of the detector area. The results given in Fig. 8(b) indicate a final off-specular relaxation time of 3.3 μs. The difference of approximately a factor 2 nicely confirms the transition from heterodyne to homodyne detection. In Fig. 8(a), we note at the transition a difference in contrast, which is larger for the heterodyne regime.

Heterodyne detection is more sensitive, as the weak quasi-elastic intensity is not modulated by itself but by the strong elastic signal. In classical dynamic light scattering, one cannot measure at the specular position, and, to take advantage of the heterodyne scheme, an artificial secondary source must be created at off-specular positions. The above discussion suggests that for X-rays the elastic intensity at the Bragg reflection or at any other specular position with enough intensity, can act as a 'natural' secondary source. This opens up new opportunities for probing the dynamics of a variety of systems that produce intense X-ray diffraction patterns, by performing XPCS measurements at Bragg reflections.

5. Conclusions

Smectic membranes can be made with an extraordinary uniformity while in addition they are very stable in the X-ray beam. In combination with the existence of low-dimensional fluctuations these properties make them very suitable for XPCS, allowing in-depth investigations of the technique. We have discussed how in XPCS experiments the coherence properties of the beam influence the time dependence of the measured intensity correlations. The basic assumption is that the coherence volume acts like a filter, selecting fluctuations of the smectic membrane with matching wavelength. Measurements at different scattering angles fully support this model. Changing the resolution of the setup by variation of the

detector slits also influences the time behavior of the correlation function. This indicates a relation with the size of the scattering volume. Both effects can be incorporated in an 'effective' resolution of the setup that accounts for both the resolution and the coherence of the beam. Clear evidence has been provided for a transition between heterodyne detection at the specular ridge and homodyne detection for off-specular scattering geometries.

Acknowledgements

The authors thank Henri Gleyzolle and Patrick Feder (ID10, ESRF) for technical support, and A.I. Chumakov (ID18, ESRF) for providing fast avalanche-photodiode detectors. This work is part of the research program of the 'Stichting voor Fundamenteel Onderzoek der Materie' (FOM), which is financially supported by the 'Nederlandse Organisatie voor Wetenschappelijk Onderzoek' (NWO).

References

[1] S. Dierker, NSLS Newsletter (July) (1995) 1.
[2] D.L. Abernathy, G. Grübel, S. Brauer, I. McNulty, G.B. Stephenson, S.G.J. Mochrie, A.R. Sandy, N. Mulders, N. Sutton, J. Synchrotron Radiat. 5 (1998) 37.
[3] D. Lumma, L.B. Lurio, S.G.J. Mochrie, M. Sutton, Rev. Sci. Inst. 71 (2000) 3274.
[4] T. Seydel, A. Madsen, M. Sprung, M. Tolan, G. Grübel, W. Press, Rev. Sci. Inst. 74 (2003) 4033.
[5] M. Sutton, K. Laaziri, F. Livet, F. Bley, Opt. Express 11 (2003) 2268.
[6] G. Grübel, F. Zontone, J. Alloys Compd. 362 (2004) 3.
[7] S.G.J. Mochrie, A.M. Mayes, A.R. Sandy, M. Sutton, S. Brauer, G.B. Stephenson, D.L. Abernathy, G. Grübel, Phys. Rev. Lett. 78 (1997) 1275.
[8] T. Thurn-Albrecht, G. Meier, P. Müller-Buschbaum, A. Patkowski, W. Steffen, G. Grübel, D.L. Abernathy, O. Diat, M. Winter, M.G. Koch, M.T. Reetz, Phys. Rev. E 59 (1999) 642.
[9] L.B. Lurio, D. Lumma, A.R. Sandy, M.A. Borthwick, P. Falus, S.G.J. Mochrie, J.F. Pelletier, M. Sutton, L. Regan, A. Malik, G.B. Stephenson, Phys. Rev. Lett. 84 (2000) 785.
[10] D.O. Riese, W.L. Vos, G.H. Wegdam, F.J. Poelwijk, D.L. Abernathy, G. Grübel, Phys. Rev. E 61 (2000) 1676.
[11] G. Grübel, D.L. Abernathy, D.O. Riese, W.L. Vos, G.H. Wegdam, J. Appl. Crystallogr. 33 (2000) 424.
[12] D. Lumma, L.B. Lurio, M.A. Borthwick, P. Falus, S.G.J. Mochrie, Phys. Rev. E 62 (2000) 8258.
[13] T. Seydel, A. Madsen, M. Tolan, G. Grübel, W. Press, Phys. Rev. B 63 (2001) 3409.
[14] J. Lal, D.L. Abernathy, L. Auvray, O. Diat, G. Grübel, Eur. Phys. J. E 4 (2001) 263.
[15] M. Tolan, T. Seydel, A. Madsen, G. Grübel, W. Press, S.K. Sinha, Appl. Surf. Sci. 182 (2001) 236.
[16] H. Kim, A. Rühm, L.B. Lurio, J.K. Basu, J. Lal, D. Lumma, S.G.J. Mochrie, S.K. Sinha, Phys. Rev. Lett. 90 (2003) 068302.
[17] A. Madsen, J. Als-Nielsen, G. Grübel, Phys. Rev. Lett. 90 (2003) 085701.
[18] S.G.J. Mochrie, L.B. Lurio, A. Rühm, D. Lumma, M. Borthwick, P. Falus, H.J. Kim, J.K. Basu, J. Lal, S.K. Sinha, Phys. B 336 (2003) 173.
[19] A. Madsen, T. Seydel, M. Sprung, C. Gutt, M. Tolan, G. Grübel, Phys. Rev. Lett. 92 (2004) 096104.
[20] B. Lengeler, Naturwissenschaften 88 (2001) 249.
[21] I.A. Vartanyants, I.K. Robinson, Opt. Commun. 222 (2003) 29.
[22] W.H. de Jeu, B.I. Ostrovskii, A.N. Shalaginov, Rev. Mod. Phys. 75 (2003) 181, and references therein.
[23] A.C. Price, L.B. Sorensen, S.D. Kevan, J. Toner, A. Poniewierski, R. Hołyst, Phys. Rev. Lett. 82 (1999) 755.
[24] A. Fera, I.P. Dolbnya, G. Grübel, H.-G. Muller, B.I. Ostrovskii, A.N. Shalaginov, W.H. de Jeu, Phys. Rev. Lett. 85 (2000) 2316.
[25] I. Sikharulidze, B. Farago, I.P. Dolbnya, A. Madsen, W.H. de Jeu, Phys. Rev. Lett. 91 (2003) 165504.
[26] I. Sikharulidze, I.P. Dolbnya, A. Fera, A. Madsen, B.I. Ostrovskii, W.H. de Jeu, Phys. Rev. Lett. 88 (2002) 115503.
[27] See, for example P.M. Chaikin, T.C. Lubensky, Principles of Condensed Matter Physics, Cambridge University Press, Cambridge, 1995.
[28] R. Hołyst, Phys. Rev. A 44 (1991) 3692.
[29] See, for example B. Chu, Laser Light Scattering: Basic Principles and Practice, Academic Press, San Diego, 1991.
[30] B. Berne, R. Pecora, Dynamic Light Scattering with Applications to Chemistry, Biology and Physics, Dover Publications Inc., New York, 2000.
[31] D. Langevin, Experimental realization, in: D. Langevin (Ed.), Light Scattering by Liquid Surfaces and Complementary Techniques, Dekker, New York, 1992.
[32] C. Gutt, T. Ghaderi, V. Chamard, A. Madsen, T. Seydel, M. Tolan, M. Sprung, G. Grübel, S.K. Sinha, Phys. Rev. Lett. 91 (2003) 076104.
[33] S.K. Sinha, M. Tolan, A. Gibaud, Phys. Rev. B 57 (1998) 2740.
[34] D. Sentenac, A.N. Shalaginov, A. Fera, W.H. de Jeu, Appl. Cryst. 33 (2000) 130.
[35] A.N. Shalaginov, D.E. Sullivan, Phys. Rev. E 62 (2000) 699.
[36] A.Q.R. Baron, Hyperfine Interactions 125 (2000) 29.

[37] C. Rosenblatt, N. Amer, Appl. Phys. Lett. 36 (1980) 432.
[38] P. Pieranski, L. Beliard, J.-Ph. Tournellec, X. Leoncini, C. Furtlehner, H. Dumoulin, E. Riou, B. Jouvin, J.-P. Fénerol, Ph. Palaric, J. Heuving, B. Cartier, I. Kraus, Phys. A 194 (1993) 364.
[39] W.H. de Jeu, A. Madsen, I. Sikharulidze, S. Sprunt, Phys. B (in press) doi:10.1016/j.physb.2004.11.016.